Technical University of Budapest
1782
Department of Fluid Mechanics

R&D (TéT) Cooperation Project I-28/98

DMA-URLS

Technical Note on

Computational investigation of flow phenomena in an isolated axial fan rotor using Navier-Stokes procedure

Alessandro Corsini

Dipartimento di Meccanica e Aeronautica – University of Rome “La Sapienza”

Abstract

A finite element based Navier-Stokes solver is applied to investigate the three-dimensional viscous flow in a low speed isolated axial rotor with tip clearance at design condition. An higher-order anisotropic eddy viscosity model is used for closure, with wall function treatment able to simulate stationary and moving boundaries. The presented comparisons with experimental data include three-dimensional flow structure behind the rotor as well as the tip leakage flow behaviour developing through the rotor. It is shown that the code predicts well the flow structure observed in the experiments. A critical discussion of predicting limits is also carried out in order to address possible improvements.

Introduction

Turbomachinery flows modeling requires built-in capabilities for the assessment of viscous and turbulent effects on secondary flows (endwall losses, flow turning, flow separation, etc.). The ordinary first moment closure turbulence model lacks of sensitivity due to the forced isotropy of normal Reynolds stress components, thus the adoption of more physical stress-strain constitutive relation scheme is needed. The computational approach, here proposed for steady incompressible internal flows, adopts a *non linear k* - e model (Craft et al., 1993) with wall function treatment of solid boundaries to preserve acceptable level of discretization.
The simulation of internal flows in Turbomachinery is here approached on the basis of modified *Galerkin* finite element (FE) formulation, developed in order to control the main instability sources that affects incompressible flows numerical prediction. The developed FE formulation is based on a *stabilized Petrov-Galerkin* method, supported on 3-D elements by mixed or equal order trial functions. The consistent stabilization scheme is tuned in order to act as discontinuous streamline balancing diffusive term in the advection-dominated flow (Brooks et al., 1982), and as an incompressibility constraint relaxing term in diffusive-dominated flow behaviour (Tezduyar, 1992). As far as the solution strategy is concerned, satisfactory computational compromise has been achieved by adopting 'in core' semi-iterative solver (*Generalized Minimal Residual - GMRes* Saad et al. 1986) with compact management of the stiffness matrix stored using addressing arrays (Borello et al., 1997b).
The developed numerical tool is here used to gain an insight into the complex three-dimensionl (3D) flow developing in an axial fan rotor of non free vortex (NFV) design, with special concern to the tip leakage flow region. The numerical model of rotor employs a conventional H-grid topology with the adoption of a 'thin blade approximation' for the tip gap (Basson et al. 1993), and the set of applied boundary conditions is based on the detailed experimental investigations carried out by Vad and Bencze (1996).
In this study, the Navier-Stokes prediction of the tested fan rotor flow is first validated against the benchmark LDA measurements on the flow field downstream of the rotor provided by Vad (1997) and Vad and Bencze (1996), (1998a). Then, the predicted tip leakage flow behaviour at the design flow rate is compared to literature experimental studies available for rotor as well as moving or stationary cascade flows. The results demonstrate the actual capabality of the proposed numerical approach for complex turbomachinery flows.
A critical discussion of predicting limits is also carried out, in order to address the possible improvements for both flow and rotor modeling.

Numerical Analysis

Model equations. The adopted numerical scheme has been implemented on the in-house developed finite-element Navier-Stokes code (Rispoli and Siciliani, 1994), (Corsini 1996), (Borello et al. 1997a), (Corsini et al. 1999).

The code solves the steady and three-dimensional Reynolds averaged Navier-Stokes equations in a rotating frame. In the following overview of the modelled equations used to describe the flow, the usual Reynolds averaging has been adopted decomposing (each quantity ϑ) $\vartheta = \overline{\vartheta} + \vartheta'$, where the overbar indicates conventional average, and the prime a fluctuation with respect to the latter. The adopted fluid dynamic closure is carried out with non Newtonian stress-strain relationship in order to recover the anisotropy of turbulent stress tensor. The Reynolds stress tensor $\overline{w'_i w'_j}$ is, thus, modeled in the form of a third order polynomial function of mean strain and vorticity tensors and of a non linear scalar turbulent viscosity μ_t, on the basis of *non linear k-*ε model proposed by Craft et al. (1993), already applied to turbomachinery flow prediction (Borello et al., 1997a).
The averaged equations (*x*-, *y*- and *z*- momentum, mass, turbulent kinetic energy *k*, viscous dissipation rate ε) are here summarized in vector form for a statistically stationary three dimensional, incompressible and turbulent flow in a rotating frame:

$$\left(\overline{w}_j \rho \overline{\zeta}_\alpha + \overline{\sigma}_{\alpha j}\right)_{,j} + \overline{f}_\alpha = 0 \tag{1}$$

with the ensuing sets of Dirichelet and Neumann conditions applied on computational domain D boundary $\partial D = \partial D_{d\alpha} \cup \partial D_{v\alpha}$:

$$\begin{aligned} \overline{\zeta}_\alpha &= d_\alpha && \to \partial D_{d\alpha} \\ -\overline{\sigma}_{\alpha j} n_j &= v_\alpha && \to \partial D_{v\alpha} \end{aligned} \tag{2}$$

and with reference to the following vector of the unknowns:

$$\left\{\overline{\vartheta}_\alpha\right\} = \left\{\overline{w}_x, \overline{w}_y, \overline{w}_z, \overline{p}, k, \varepsilon\right\}^T = \left\{\overline{\zeta}_\alpha\right\} + \left\{0, 0, 0, \overline{p} - 1, 0, 0\right\}^T \tag{3}$$

The diffusive flux tensor $\left\{\overline{\sigma}_{\alpha j}\right\}$ and the residual forces vector $\left\{\overline{f}_\alpha\right\}$ are defined as:

$$\left\{\overline{\sigma}_{\alpha j}\right\} \equiv \left\{\overline{\tau}_{xj}, \quad \overline{\tau}_{yj}, \quad \overline{\tau}_{zj}, \quad 0, \quad -\left(\mu + \mu_t/\Gamma_k\right)k_{,j}, \quad -\left(\mu + \mu_t/\Gamma_\varepsilon\right)\varepsilon_{,j}\right\}^T \tag{4}$$

where $\overline{\tau}_{ij} = \overline{p}^* \delta_{ij} - \mu_m(\overline{w}_{i,j} + \overline{w}_{j,i})$, with $\overline{p}^* = \overline{p} + (2/3)\rho k$, and:

$$\left\{\overline{f}_\alpha\right\} \equiv \left\{\overline{f}_{inx} + \overline{P}_{mx}, \quad \overline{f}_{iny} + \overline{P}_{my}, \quad \overline{f}_{inz} + \overline{P}_{mz}, \quad 0, \quad -\overline{P}_k + \rho\varepsilon, \quad -c_{\varepsilon 1}\frac{\varepsilon}{k}\overline{P}_k + c_{\varepsilon 2}\rho\frac{\varepsilon^2}{k}\right\}^T \tag{5}$$

The effective transport coefficients, accounting for both the molecular and turbulent transport mechanisms, are:

$$\mu_m = \mu + \mu_t, \qquad \mu_k = \mu + \mu_t/\Gamma_k, \qquad \mu_\varepsilon = \mu + \mu_t/\Gamma_\varepsilon, \tag{6}$$

where the non-linear turbulent viscosity is expressed as:

$$\mu_t = \rho c_\mu \frac{k^2}{\varepsilon}, \qquad \text{with} \qquad c_\mu = \frac{0.3 \cdot \left[1 - exp\left[-0.36 / exp\left(-0.75\, max(S, \Omega)\right)\right]\right]}{1 + 0.35\, max(S, \Omega)^{1.5}},$$

thus depending on the invariant parameters strain S and vorticity Ω:

$$S = \frac{k}{\varepsilon}\sqrt{\frac{1}{2}S_{ij}S_{ij}} \qquad \Omega = \frac{k}{\varepsilon}\sqrt{\frac{1}{2}\Omega_{ij}\Omega_{ij}} \tag{7}$$

where $S_{ij} = (\overline{w_{i,j}} + \overline{w_{j,i}})$ is twice the mean rate of strain tensor, and $\Omega_{ij} = \left(\overline{w}_{i,j} - \overline{w}_{j,i}\right) + 2e_{ijm}\omega_m$, is twice the absolute vorticity tensor. The eddy viscosity model constants are token as:

$$G_k = 1.0, \quad G_e = 1.3, \quad c_{e1} = 1.44, \quad c_{e2} = 1.92$$

In the implemented closure the anisotropic Reynolds stress tensor, resulting from the *non linear* constitutive relationship, contributes to the momentum equations acting both as diffusive fluxes Newtonian like (with its first order term), and as local source of momentum (originating from the divergence of second and third order terms) (Corsini, 1996).

Numerical scheme. The finite element formulation adopts a *Stabilized Petrov Galerkin Method*, modified for the application to 3D elements. The stabilization technique involves a perturbation of the functions used to weight the advective-diffusive equations, acting as a discontinuous artificial contribution in the streamline direction (*Streamline Upwind Petrov Galerkin* term (Brooks and Hughes, 1982), (Borello et al., 1997b)), and a perturbation of the continuity weights, acting as relaxation of incompressibility constraint proportional to a Laplacian pressure term (*Pressure Stabilized Petrov Galerkin* term (Tezduyar, 1992), (Corsini, 1996) (Borello et al., 1997b)). The resulting non linear discrete system is linearized by the use of relaxed successive substitutions, and is solved by an iterative solution procedure *GMRES* based (Saad and Schultz, 1986), (Borello et al., 1997a).

Computational grid. The test fan consists of *12* straight (unswept) cambered plate blades, with constant chord of *171 mm*. The average chordwise tip clearance is $c = 3$ *mm* and the maximum blade thickness is *2 mm*. Further details of the design characteristics and fan geometry can be found in (Vad and Bencze, 1998a).

To represent the domain defined by blade geometry and tip clearance, non orthogonal body fitted coordinates have been generated. The grid consists of $59 \cdot 21 \cdot 31$ nodes in streamwise, blade to blade and spanwise direction respectively (Fig. 1). The stretching toward solid boundaries is modulated to set the first grid node inside the inertial sublayer, limiting its dimensionless distance from the solid boundaries in the range $30 < d^+ < 200$. In particular, the first grid node in the tip gap has been located *0.002* chords away from the wall. The validity of *thin blade* approximation allows the use of H-grid topology, also in modelling the clearance region *via* the 'pinching' of blade tip grid points (Fig. 1). Such simple approach, though responsible of an high skewing of the mesh in the tip clearance and of an approximate geometric representation, allows an easy implementation of tip gap boundary conditions (periodicity) and is suitable for simulating tip clearance flow behaviour providing good engineering approximation, see Basson and Lakshminarayana (1995), Storer and Cumpsty (1991), Goyal and Dawes (1993), Corsini et al. (1999).

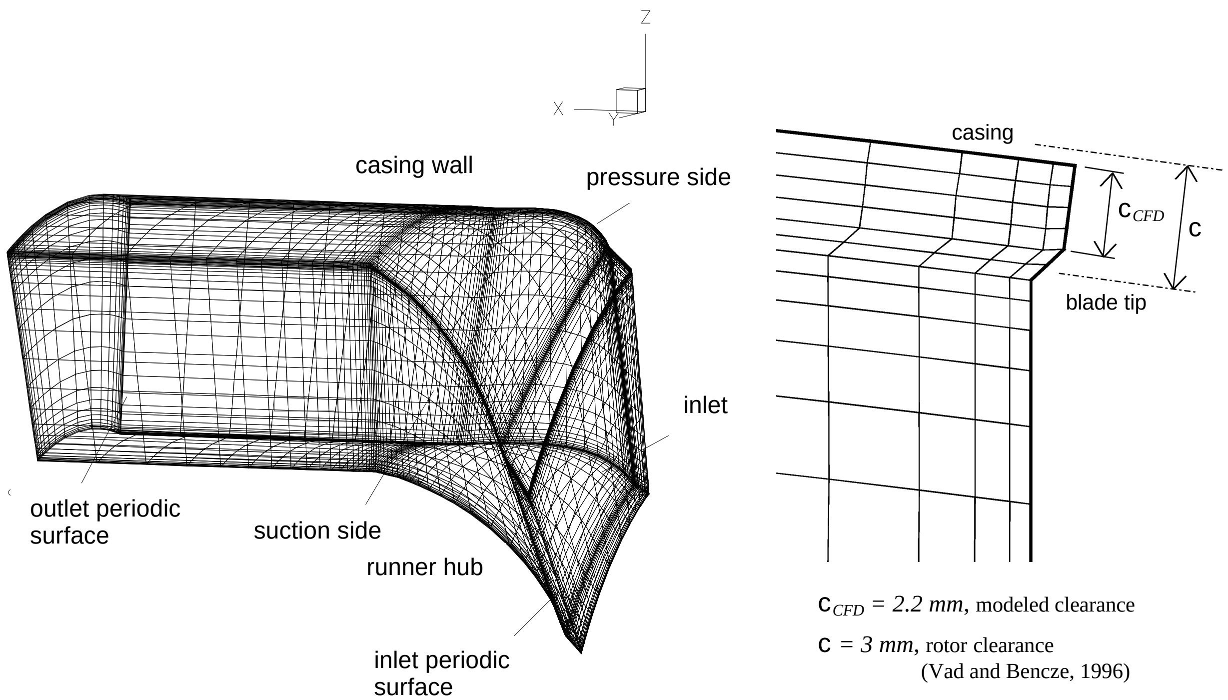

Fig. 1: Computational grid and tip gap grid detail

Boundary conditions. The boundary conditions were token from measurements were possible. The inlet Dirichelet conditions for the relative velocity components are obtained from the LDA upstream measurements, which clearly show the influence of inlet nose cone curvature and the rotor sucking effect near the tip flow region (Fig. 2). The distribution of the turbulence kinetic energy at the inlet is obtained from axi-symmetric turbulence intensity profile derived on the basis of the upstream LDA data provided by Vad (1999). The turbulence intensity (*TI*) profile (*TI* is defined as the root mean square of three normal stresses normalized by the casing relative peripheral velocity U_c: $TI = \sqrt{2k/3}/U_c$) shows a nearly uniform value in the core region (about *6* percent) and it grows markedly in the proximity of the endwalls (near the hub about *10* percent and the peak value of *15* percent at the higher radii). The inlet profile of turbulence energy dissipation rate is based on the characteristic length scale definition (*0.01* of rotor pitch at midspan) (Hah 1986). As far as the treatment of near wall regions is concerned, an analytical description of the boundary layer has been adopted in order to avoid the concentration of a large share of computational nodes in this region of steep velocity gradients. Such a scheme model the boundary layer action *via* the computation of shear stress depending from prescribed logarithmic velocity profile within the layer normal to the solid boundaries. The effect of moving casing wall, consequence of relative rotor flow field description, is transmitted through the shear stress acting as non zero limit in the integration of velocity profile across the layer. The periodic conditions are strictly imposed at the permeable inlet and outlet boundary surfaces, and inside the tip clearance to ensure cyclic flow behaviour. Furthermore in the outlet region Neumann conditions are specified, imposing homogeneous fluxes of k and ε and non homogeneous for the static pressure.

Rotor flow numerical prediction

The flow phenomena developing in the test fan blading have been numerically investigated. In order to look for a deeper analysis of the proposed CFD tool, the predicted rotor flow is presented first in order to verify its capability of simulating the 3D flow structure downstream of the rotor, including velocity profiles, work input, losses, and secondary flows. Such comparisons have been carried out against the available LDA data (Vad and Bencze, 1996), (Vad 1997). In order to carry out a deeper analysis of the FE-CFD technique validity, the simulated detailed flow behaviour in the proximity of rotor tip gap is therefore compared against literature data available for compressor rotors (Inoue and Kuroumaru, (1984) and (1989)) and linear stationary cascade with clearance (Storer and Cumpsty, 1991). Details concerning the design specifications for the investigated rotor as well as for the benchmark rotors are summarized in Appendix. The comparisons have been focused on the capability of the proposed computational technique in predicting valid flow behaviour in realistic, decelerating and rotating cascades and as a survey on the possibilities for its improvement. In the following, flow phenomena are identified and an overview on the physics of fluid dynamical processes developing in the axial rotor under investigation is given.

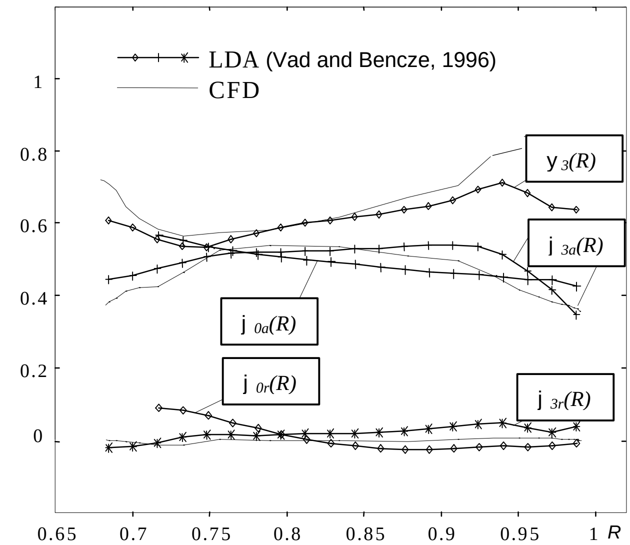

Fig. 2: Pitchwise-averaged inlet ($_0$) and outlet ($_3$) flow data

Tangentially averaged flows downstream of rotor. The simulated 3D flow structure behind the rotor is validated against the LDA data set supplied by Vad (1997) and Vad and Bencze (1996). Pitchwise-averaged flow properties are of great importance from the designer's viewpoint since they correspond to 2D stationary cascade measurement data on which the cascade design method is based. The spanwise distributions of pitchwise averaged local ideal total head rise coefficient (defined as $\psi_3 = 2R\ (v_{3p}/U_c)$ assuming zero inlet swirl) and flow coefficients (axial $\varphi_{3a} = v_{3a}/U_c$, and radial $\varphi_{3r} = v_{3r}/U_c$) at rotor outlet are shown in Fig. 2. The same picture contains also the inlet pitch-averaged axial and radial velocity profiles LDA measured upstream of the rotor, and used as inlet boundary condition for the CFD calculation. Fig. 2 shows a strong distraction effect on the inlet flow by the nose cone, resulting in spanwise changing axial velocity values and outward radial flow. This experience calls attention to consider the effect of nose cone when assuming an inlet condition in rotor cascade design. A slight forward effect of rotor blade leading edges manifests itself in locally decreased absolute values of inlet axial and radial velocities. Concerning the downstream flow, the experimental data show a slight overturning (increased swirl) near the hub, due to the effect of passage vortex driven by curvature effects near the blade root. According to the spanwise increasing ideal total head rise, the measured outlet swirl also increases with radius and it decreases eventually near the casing (underturning), due to the stationary casing wall.

The CFD swirl data are in good agreement with the measurements, except for the zone near the blade tip where drastically increased swirl can be observed. The measurements of Vad and Bencze (1996) represent lifelikely the displacement zones near the annulus walls, characterised by decreased axial velocity. This basic tendency is reflected also by the CFD results, though the displacement (axial velocity reduction) effect is overestimated near the annulus walls by the numerical simulation and the location of maximum axial velocity is shifted to lower radii. In Fig. 3 is presented a zoom of total head rise coefficient distribution at higher radii. Such a detail shows clearly that the predicted defect of absolute peripheral velocity is under-estimated, and an appreciable reduction of the coefficient is confined to the very proximity of the blade tip radius and the clearance gap. Thus the predicted flow in the annulus region leaves the blading with low relative dynamic head as if no influence of the leakage flow was computed, in clear contradiction with the measurements. In Fig. 4 is furthermore shown the pitch-wise averaged distribution of total pressure loss coefficient over a span. The plot shows that the predicted extra-work at the higher radii corresponds to a steep growth of losses, and as a consequence the flow processes is increasingly less efficient.

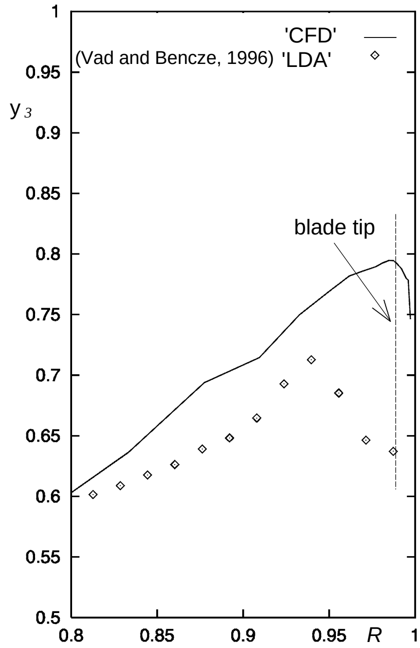

Fig. 3: Pitchwise-averaged outlet (3) distribution of ideal total head rise coefficient. Detail of near casing region

Resolved flows downstream of rotor. As far as the pitchwise resolved experimental (Vad, 1997) and numerical flow representation data are concerned, in order to obtain a lifelike information on the flow structure downstream of the rotor the ensuing data are represented: the axial flow coefficient distribution (Fig. 5), the ideal total head rise coefficient distribution (Fig. 6), the radial flow coefficient distribution (Fig. 7), the secondary flow vector plot (Fig. 8), and the turbulence level contour plots (Fig. 9). Such figures refer to a rectangular images of the annular sector of LDA measurement and CFD computational region. The blading moves from 'the left to the right' (pressure side on the left, suction side on the right within the blade passage downstream region). The rotor hub is on the bottom and the casing wall is on the top. The local axial flow coefficient j $_{3a}$ contour plots are shown in Fig. 5. The blade wake (W) is indicated properly by reduced axial velocity in the computed flow field. The CFD results seem also to predict a wider high axial velocity side region (S) near the blade wake, in which the velocity grows according to a blockage effect caused by the modeled suction side blade boundary layer. The zone of increased axial velocity near the casing wall on the pressure side is larger in the CFD prediction and extended up to an unphysical spanwise position. The lag in axial velocity near the casing wall (C) is well predicted except in the vicinity of blade pressure side. As well is realistically simulate the lag in the tip region (T) where the leakage flow interacts with NFV flow, although with a wider 'in-passage' extension. Such low axial velocity zone is mainly responsible for the appearance of the casing wall displacement layer in Fig. 2, whose extension is overestimated in the CFD simulation. At the lower radii, the computed plot indicates the presence of separate passage vortex trace (PV) and blade root suction side stall zone (ST).

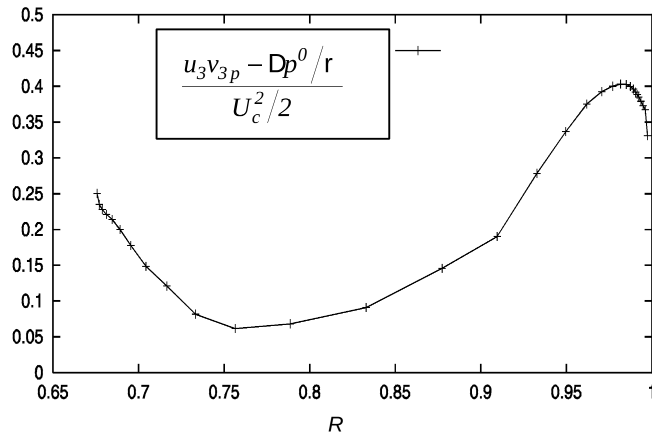

Fig. 4: Predicted pitchwise-averaged outlet ($_3$) distribution of total pressure loss coefficient

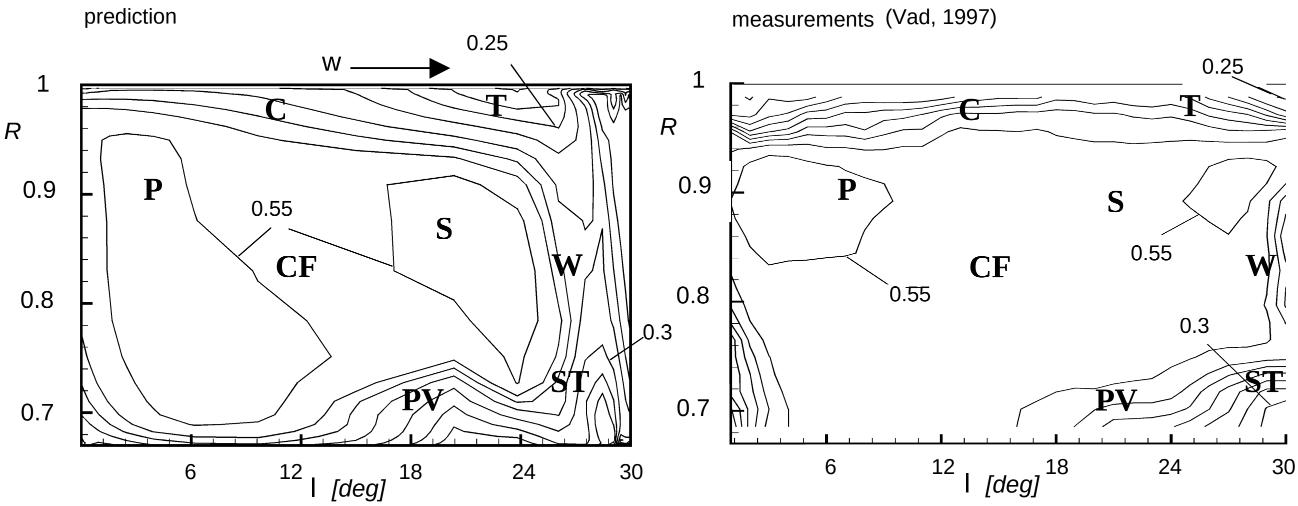

Fig. 5: Contour plots of outlet axial flow coefficient
a. predictions
b. measurements (Vad, 1997)

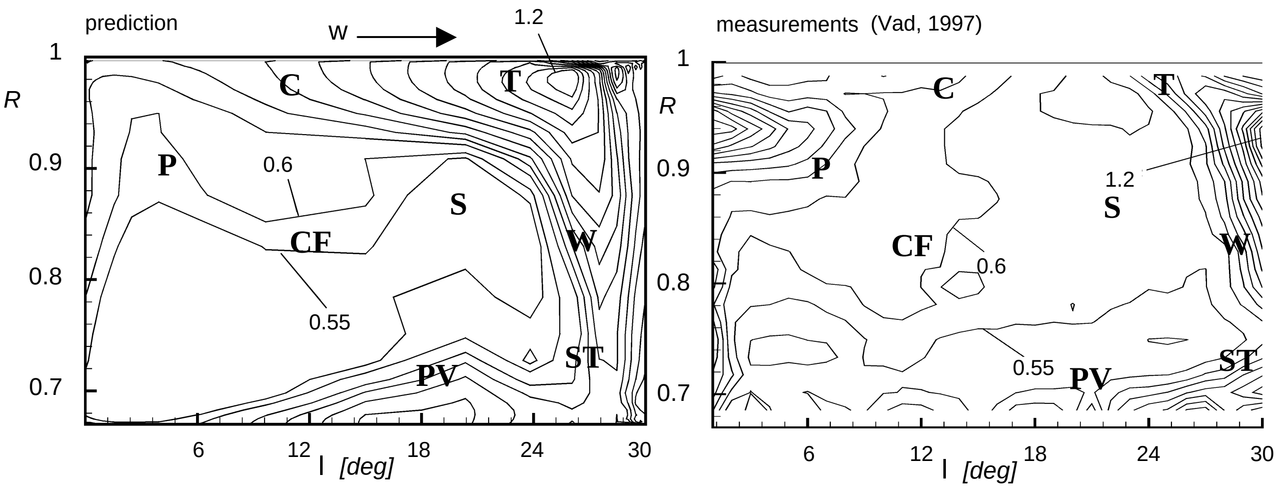

Fig. 6: Contour plots of outlet ideal total head rise coefficient
a. predictions
b. measurements (Vad, 1997)

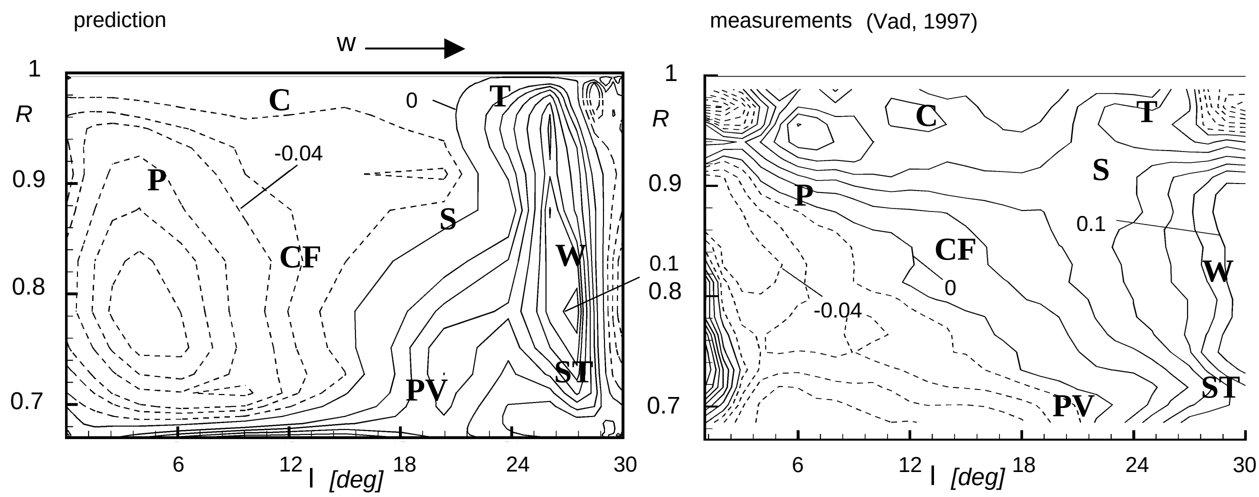

Fig. 7: Contour plots of outlet radial flow coefficient
a. predictions
b. measurements (Vad, 1997)

Though a good agreement of computed flow field against measurements of Vad (1997) is obtained, still remain problems such as the prediction of the wake (W) and the displacement of the hub vortical structures toward the inner portion of the pitch. In Fig. 6, the resolved ideal total head rise coefficient distribution is presented.

The predicted distribution seems to confirm the conclusions already drawn above. In detail, the wake (W) and the hub region (PV and ST) seem correctly predicted, with a fair quantitative agreement. The displacement effect of suction side blade boundary layer is also confirmed by a small pitch-wise wake extension. A lack of agreement appears clearly in comparing the casing flow region. The predicted flow accumulates in a discrete core with low relative dynamic head that spreads toward the middle of the pitch. As already mentioned concerning the pitch-averaged data (Fig.s 2, 3), the predicted behaviour show the decay of leakage flow influence (underturning effect) at the aft part of the blade. Whereas the leakage flow effect appears strongly in LDA measurements, enforcing the NFV vortex structure and washing the annulus region. With concern to such a predictive fault, it is worth to note that the dynamic head within the core is too deep to be related to the prediction of an over-swepting of the collateral inlet boundary layer. Adopting the hypothesis of local axial velocity uniformity between the leading and the trailing edges, a theoretically estimate of the minimum relative dynamic head could be obtained adding the peripheral dynamic head of a fluid particle very close to the blade tip (about $0.5\ (U_{tip})^2$) to the local axial dynamic head. Therefore the expected dynamic head in the core of the high-loss region is about *0.6* at design condition. Instead the measured (about *0.55*) and predicted values (minimum of about *0.52*) are less than this, as if the core region represents the down-stream evidence of the decayed leakage vortex structure. As a consequence of the described behaviour, in Fig. 7, the radial flow coefficient distribution does not show any trace of the vortex structure close to the tip (within the region of interaction between the radial outward flow and the leakage one).

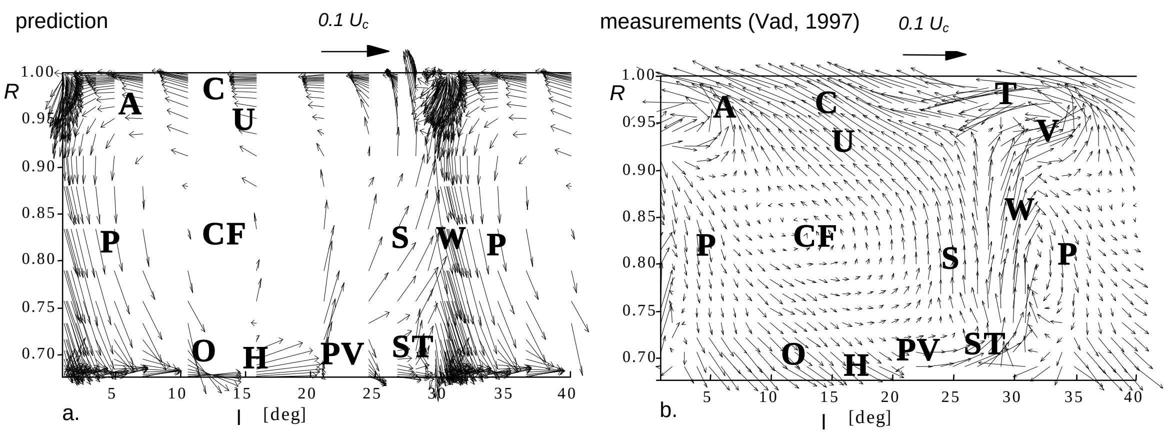

Fig. 8: Secondary flow vector diagram at rotor outlet (Corsini et al., 1999)
a. predictions
b. measurements (Vad, 1997)

Using the definition and calculation method of e.g. Inoue et al. (1991), the secondary flow was obtained as a velocity component perpendicular to the relative theoretical flow direction. Theoretical flow was considered as an ideal 2D flow pattern corresponding to the design concept and supported by two-dimensional stationary cascade measurement data (Vad and Bencze (1998)). As shown by Vad and Bencze (1996), the vortical NFV flow pattern filling the largest part of the LDA measurement range can be observed with a single glance in Fig. 8. It consists of suction side outward (S) and pressure side inward (P) radial flow branches, linked with an overturning zone (O) near the hub and an underturning zone (U) near the casing wall and enclosing a central flow region (CF). Blade wakes (W) of low relative kinetic energy, a vortical phenomenon near the blade tip (V), flow in the blade tip region (T), a viscous flow region on the casing wall (C), fluid of low relative kinetic energy accumulating near the pressure side blade tip (A), stall zone in the suction side blade root - hub wall corner (ST), viscous region on the hub wall (H), and a passage vortex (PV) are also distinguished.

The CFD data represent satisfactorily the NFV flow (S, P, O, U, CF zones) indicating that the applied computational method is capable principally for flow prediction in a NFV operational state (in terms of both the theoretical streamline position and the radial velocity component values). As the LDA experiments of Vad (1997) show, a radial outward flow dominates in the blade wake (W) region due to centrifugal effects. In the CFD data, a smaller pitchwise extension of such radial outward region is apparent and, because of the underestimation of leakage flow intensity, no coherent vortex structure could be find in the predited suction side tip region.

Fig. 9 shows the contour map of the turbulence intensity at the measuring section. The computational data are here compared against the measurement carried out by Inoue and Kuroumaru (1984) on isolated free vortex axial

flow compressor rotor. The turbulence intensity is normalized by the blade tip velocity.
The qualitative comparison clearly shows a fair agreement in predicting the blade boundary layer regions, together with the corner zone on the suction side. Near the casing the core with the highest turbulence level (with a radial extension in the range (*0.95 R* , *0.99 R*) seems to correctly predict the presence of a region of interaction between the suction side outward radial flow and the leakage jet (see Fig. 5). On the hub wall qualitative differences still remain and the high turbulence level core (*TL = 0.8*) is related with the (PV) vortex coherent structure already shown (see Fig.s 5 and 8).

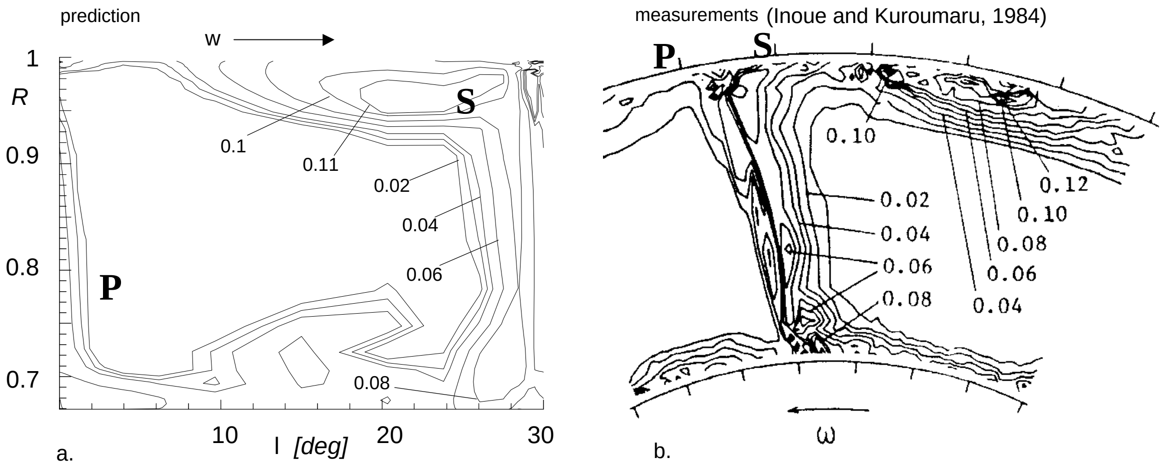

Fig. 9: Turbulence level contour plot at rotor outlet.
a. predictions on axial fan rotor designed by Vad and Bencze (1996)
b. measurements from Inoue and Kuroumaru (1984) (reprinted with permission of ASME)

Endwall boundary layers integral properties. In order to complete the analysis of the downstream behaviour of flow field in NFV rotor, attention have been given to the casing wall boundary layer and its integral properties are here evaluated. The development of annulus boundary layers is a critical challenge for the CFD technique, for such reason the following integral parameters have been investigated:

the axial displacement thickness,

$$\delta_a = \int_0^\delta \left(1-\frac{v_a}{v_a^e}\right)dn \tag{7}$$

the axial momentum thickness,

$$\theta_a = \int_0^\delta \left(1-\frac{v_a}{v_a^e}\right)\frac{v_a}{v_a^e}dn \tag{8}$$

the tangential force deficit,

$$f_p = \int_0^\delta \left(1-\frac{v_a v_p}{v_a^e v_p^e}\right)dn \tag{9}$$

The position of boundary layer edge (δ) normal to the casing wall has been conventionally taken where the axial velocity v_a reaches its maximum value v_a^e, and $f_p^e = v_a^e v_p^e$ is the tangential force value at that position. The shape factor is defined as: $H = \delta_a / \theta_a$. The comparison of casing wall boundary layer integral properties predicted and measured for the rotor of Vad and Bencze (1996) is summarised in Tab. 1. The same table shows the value of the endwall blockage factor defined as:

$$K_B = \frac{(r_c-\delta_{ac})^2-(r_h+\delta_{ah})^2}{r_c^2-r_h^2} \tag{10}$$

where r_c, δ_{ac} and r_h, δ_{ah} are respectively the casing and hub wall radius and axial displacement thickness.

Summary of casing wall boundary layer integral parameters (axial fan rotor designed by Vad and Bencze, 1996)			
	predicted	**measured**	
δ_a (mm)	11.4	11.4	upstream
δ_a (mm)	3.3	2.7	downstream
q_a (mm)	2.6	2.1	
H	1.27	1.3	
K_B	0.92	0.95	

Tab. 1: *Casing wall* boundary layer integral parameters upstream and down stream of the rotor

The first thing to draw attention is the thickness of the casing boundary layer at the inlet section of the blading, as measured by Vad and Bencze (1996). The thickening of the boundary that enters the rotor could be related to the influence of inlet nose cone, which introduces a sudden cross section reduction with a strong distortion of the uniform axial flow (as already shown discussing Fig. 2). The measured axial development of the casing wall boundary layer confirm the typical behaviour for a small tip clearance, that is the displacement of the layer experiences a pronounced thinning in order to satisfy a 'natural' outflow condition determined by the blading (Hunter and Cumpsty, 1982). Experimentally the d_a reduces from upstream to downstream with an approximate ratio of *1/4*, while the prediction shows a thinning ratio of *1/3*, that is just greater. Although such difference, the measured and computed boundary layer shape factor *H* are in good agreement giving a twofold confirmation: the computed casing wall layer is fully turbulent and the synthetic wall treatment is substantially able to predict the shape of velocity distribution in a turbulent layer. Such circumstance could be explained as an effect of the high momentum contents predicted within the boundary layer. From a design viewpoint, the analysis of flow integral properties, shows also that a slight overestimation of the predicted blockage effect.

Wall static pressure field in the rotor blading. The analysis of static pressure distributions on the blade surfaces is here also discussed. Although no measurements have been carried out on the simulated test rotor (Vad and Bencze, 1996), such analysis defines a critical verification step because of the role that the pressure gap between the tip clearance plays on the leakage phenomena. As stated by the simple Rains' model and as shown by the previous work of Storer and Cumpsty (1991), the static pressure field controls in practice the chordwise distribution of tip leakage flow, and the effect of viscosity within the tip gap has a little magnitude.

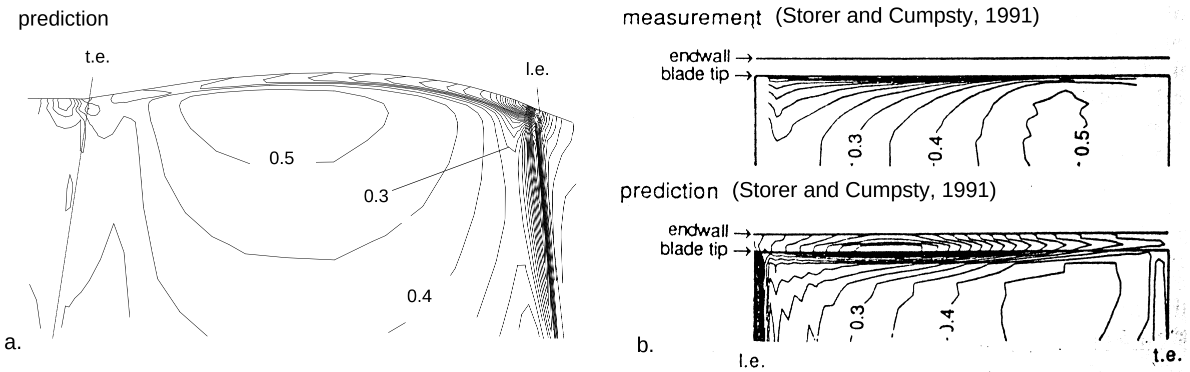

Fig. 10: Blade surface static pressure distribution (C_p) - pressure side
a. predictions on axial fan rotor designed by Vad and Bencze (1996)
b. measurements and predictions on linear cascade from Storer and Cumpsty (1991) (reprinted with permission of ASME)

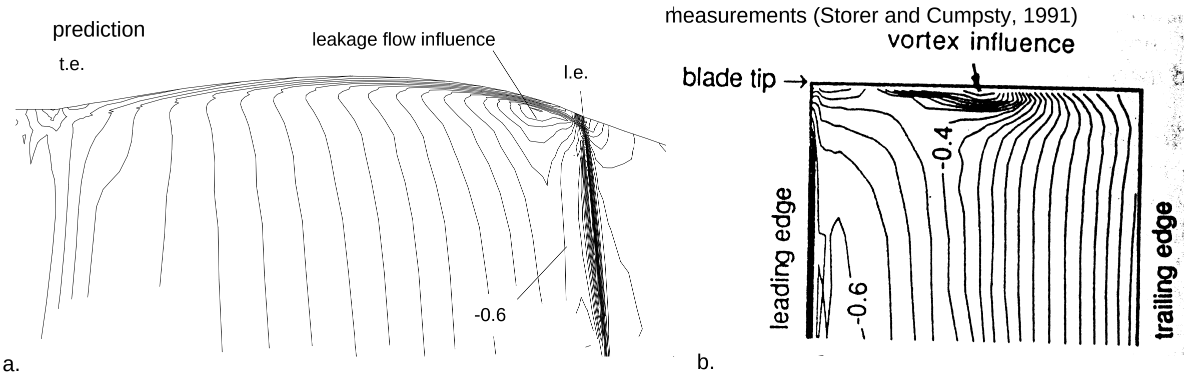

Fig. 11: Blade surface static pressure distribution (C_p) - suction side
a. predictions on axial fan rotor deisgned by Vad and Bencze (1996)
b. measurements on linear cascade from Storer and Cumpsty (1991) (reprinted with permission of ASME)

The qualitative verification step has been, therefore, arranged comparing the previous CFD prediction against the measurements carried out by Storer and Cumpsty (1991), in the case of a linear stationary cascade with tip clearance. The work of Storer and Cumpsty (1991) has been furthermore chosen as a meaningful benchmark because it presents a series of computational results obtained with the finite volume based code developed by Dawes (1987). Fig. 10 shows the static pressure distribution ($C_p = (\bar{p} - \bar{p}_1)/0.5\, r\, U_c^2$) on the blade pressure surface in the proximity of the tip, the predicted contours (referring to the test rotor with c/ℓ_{ch} of approximately *2* percent) are compared with both the measurements and the computational results carried out by Storer and Cumpsty (1991) on a linear cascade with c/ℓ_{ch} equal to *4* percent. In Fig. 11 the same comparison is extended to the static pressure distribution on the blade suction surface.

Although strong differences exist between the compared flow conditions, a fair qualitative agreement is clearly shown in Fig.s 10 and 11 and the proposed CFD procedure demonstrates its capability of predicting the overall physical behaviour of the investigated flow phenomena. On the blade surface pressure side (Fig. 10) the streamwise pressure gradient at the leading edge is correctly predicted, while the one across the tip (with a magnitude that is comparable to the gradient that origins from the matching between the blades and the entering flow) takes place at a chordwise position nearer to the leading edge (about *15* percent of chord lenght) according to the reduced normalized gap height (Storer and Cumpsty 1991). On the blade suction side (Fig. 11), the pressure distribution is hardly influenced by the leakage flow which reaches its highest intensity in the minimum pressure core shown in Fig. 11 (taking place at the chordwise position where a vortex structure should originate).

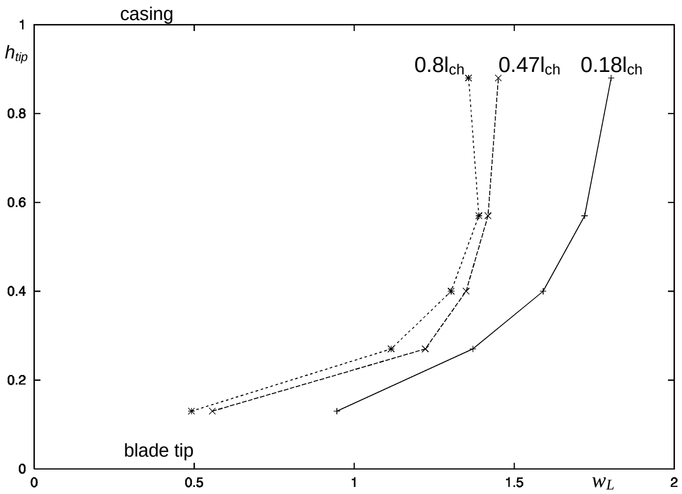

Fig. 12: Predicted velocity field leaving the tip gap

Leakage flow field inside rotor. The tip leakage flow is mainly characterized by the gap inlet and exit velocities, and the blade static pressure distributions along the tip surface. A deep insight into the predicted leakage flow phenomena is carried out in Fig.s 12 and 13, where are shown the distribution within the gap height of both the relative leakage velocity, and the relative flow direction within the gap measured with respect to the axial one. The distributions along the gap height (h_{tip} is the fraction of gap c from the blade tip) of leakage flow parameters are made at three different chordwise position, respectively: $0.18\ell_{ch}$, $0.47\ell_{ch}$, and $0.8\ell_{ch}$. In Fig. 12 the leakage velocity $\bar{w}_L$ is defined, following the conventional

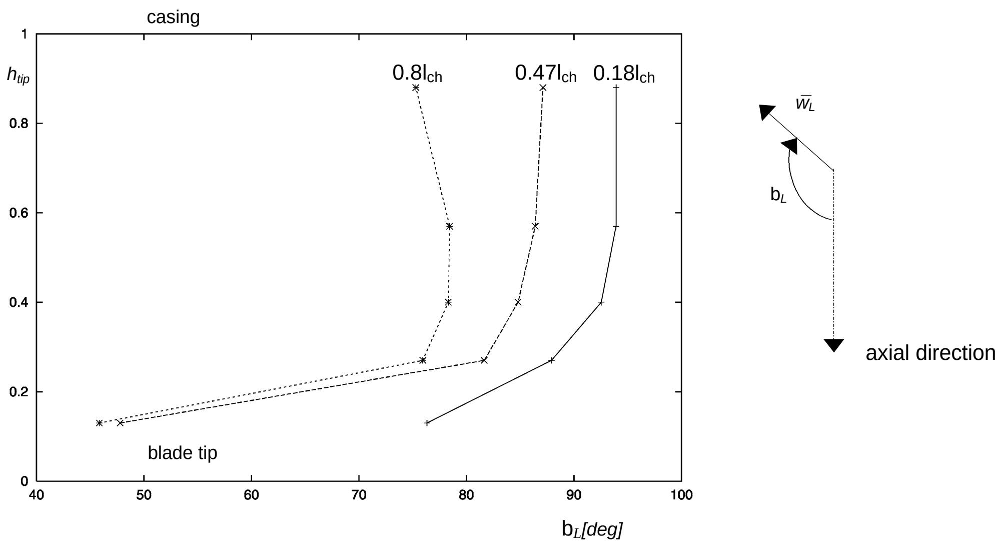

Fig. 13: Predicted flow direction leaving the tip gap

definition of Rains, as that component normal to the blade camberline (tracing the periodic boundary within the clearance) and normalized by the inlet velocity of the relative free stream. Fig. 12 shows the appearance of a distinct jet of fluid, emerging from the minimum pressure location (approximately at $0.18\ell_{ch}$) with a marked reduction of strength at all the downstream locations. Such characteristic in disagreement with the experimental observations, implies that the strength of the predicted leakage flow phenomena is weaker than the physical ones and leads to a large underprediction of the mass flow through the gap. The flow direction (Fig. 13) reaches its maximum deviation close to the minimum pressure core, and then decay markedly toward the aft of the blade (with *30* percent of reduction in the core of the jet from *0.18* to *0.8* of chord length). The predicted maximum leakage flow deviation appears underestimated if compared to the experimental data of Storer and Cumpsty, where the measured deviation reaches a magnitude of about *120 deg*. Furthermore, Fig. 13 clearly shows the formation of a leakage jet bounded by the blade tip effect, that leads to the formation of a free shear layer up to about the *25* percent of the tip gap in agreement with the measurements (Storer and Cumpsty, 1991). The flow direction, approximately constant in the core, changes as much as *20 deg* over the thickness of the shear layer apparently according to the already mentioned numerical underestimation of flow deviation.

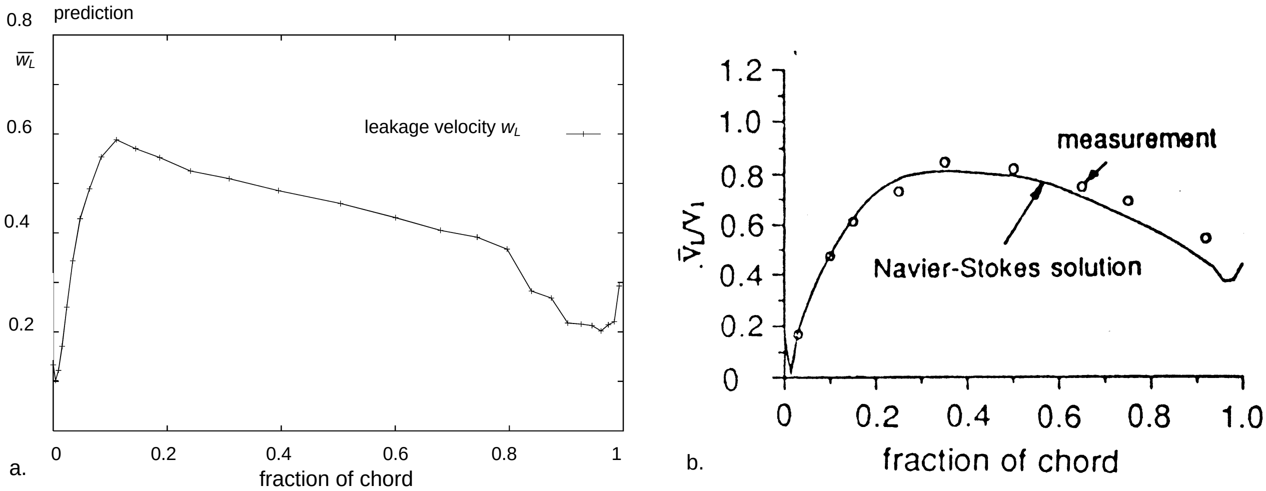

Fig. 14: Chordwise distribution of tip leakage flow averaged across the tip gap height
a. predictions on axial fan rotor designed by Vad and Bencze (1996)
b. measurements and predictions on linear cascade from Storer and Cumpsty (1991)
(reprinted with permission of ASME)

To synthetize the analysis of leakage phenomena and attempt a quantitative validation of the FE-CFD simulation is also presented, in Fig. 14, the comparison between the predicted chordwise distribution of area-averaged leakage velocity $\overline{w_L}$ against both the measurements and predictions carried out by Storer and Cumpsty (1991) for a linear stationary cascade with the tip clearance set to *2* percent of chord.

The analysis of Fig. 14 clearly confirms that, although the minimum pressure position is correctly predicted (close to *20* percent of chord length from the leading edge), the averaged leakage velocity decays rapidly due to the underestimation of leakage mass flow. In other words, the gap pressure loss related to the pinching technique of the blade tip seems to be greater than the experimental one.

Pressure on the *casing* wall. In order to complete the analysis of leakage flow behaviour, the static pressure distribution (C_p) at the casing wall is here presented and compared with the data supplied both by Inoue and Kuroumaru (1989) for an isolated axial rotor with tip clearance set to *2* percent of mid-span chord length and by Storer and Cumpsty (1991) for a linear cascade with approximately the same non-dimensional tip clearance (Fig. 15). First of all attention should be drawn to the good qualitative agreement between the CFD prediction and the benchmark experimental and numerical data (Storer and Cumpsty, 1991), (Inoue and Kuroumaru, 1989).

The presence of a vortex structure is confirmed by the prediction of a trough of pressure, that origins from the lower pressure core and manifests itself as a bent contour (already shown in Fig. 10). The position of the minimum pressure contour seems to have an evident 'in-passage' location that can be explained as an effect of the flowfield rotation (Inoue and Kuroumaru, 1989), (Moyle, 1989). The pressure trough rapidly disappears as shown by the isobars behaviour (Fig. 15), where the bend attenuates on each contour in the downstream direction. Such a behaviour could be apparently linked to the underestimation of leakage mass flow along the chord, so that the vortex formation is not sufficiently strengthened. The proposed FE Navier-Stokes technique is however able to establish the correct location of minimum pressure contour together with its trough.

FE-CFD technique predicting limits and conclusions

Some brief conclusions may be extrapolated on the basis of the above comparisons.

A three-dimensional FE Navier-Stokes procedure has shown good capabilities of predicting many aspects of 3D flow developing in axial rotors. In order to obtain an improved quantitative agreement between CFD data and experiments, two main factors have been considered: the flow field geometrical model (e.g. clearance space); the endwall and the blade boundary layer modeling.

As far as the disagreement in the clearance region is concerned, the present Navier-Stokes solver uses a very crude representation of the blade tip, in which the gap is defined by a single point. As it stands, such approximate geometrical model of the tip is not able to solve the flow in the clearance space accounting for the blade thickness influence. Such limit is strengthened by the use of the synthetic treatment of casing wall, that fails in the prediction of physical velocity and force defect within the layer and also in simulating the correct thinning of

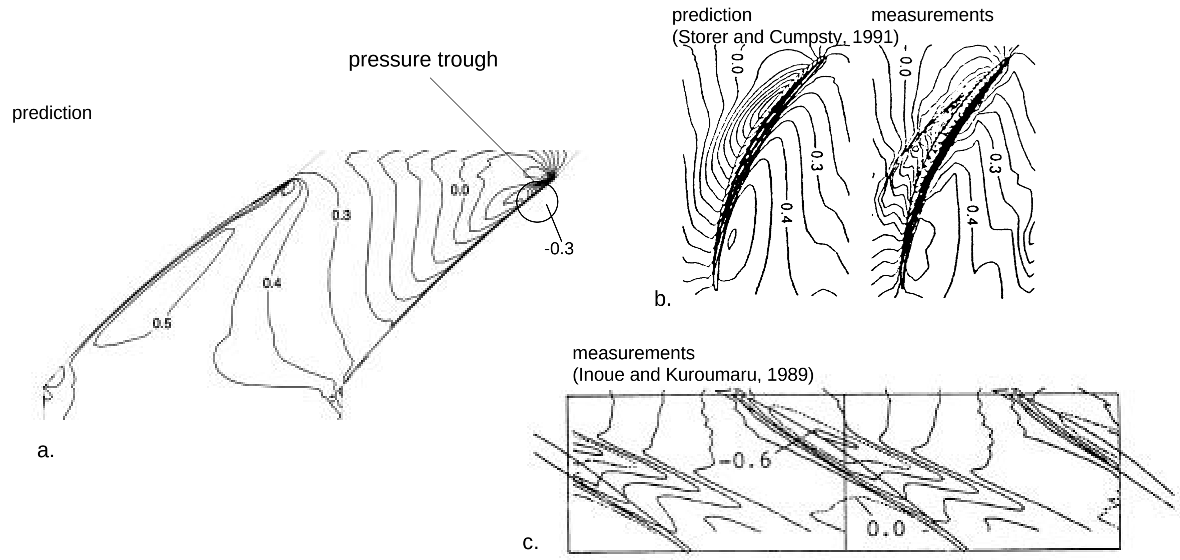

Fig. 15: Endwall static pressure distributions (C_p)
a. predictions on axial fan rotor designed by Vad and Bencze (1996)
b. measurements and predictions on linear cascade from Storer and Cumpsty (1991) (reprinted with permission of ASME)
c. measurements on axial rotor from Inoue and Kuroumaru (1989) (reprinted with permission of ASME)

casing wall displacement thickness. Early computational works (Storer and Cumpsty, 1991) (Basson et al. 1991), demonstrate that the 'pinched' blade tip modeling gives a satisfactory simulation of the leakage flow governed primarily by inviscid effects when the endwall region is solved with a Low-Reynolds turbulence model (such as the simple Baldwin-Lomax first order closure).

For such a reason it could be concluded that the weakness of the Navier-Stokes procedure implemented by the authors appears to be related to a computational reason. As a matter of fact the synthetic wall treatment simulates the effect of the relative casing motion applying an explicit shear-stress integral, a Neumann like condition weaker than the direct application of Dirichelet condition on casing wall velocity (for instance applied with a Baldwin-Lomax modeling). Together with the above mentioned the CFD computation is, furthermore, affected by the coarsening of the grid in the 'in-passage' region close to the blade surfaces. As a matter of fact the adopted grid is only suitable for an approximate determination of blade static pressure distribution (that is the primary clearance flow controlling factor), and as a consequence fails in predicting the blade force.

Concerning the rotor wake flow in the proximity of the hub, the unsophisticated blade boundary layer modeling is unable to simulate Coriolis driven stabilizing and destabilizing effects, on suction and pressure side boundary velocity profiles. Such limit apparently causes the disagreement between LDA measurements (Vad and Bencze, 1996) and CFD results (e.g. in the prediction of suction side blockage effect as well as of the displacement of wake structure from the blade surfaces toward the 'in-passage').

Acknowledgements

The work has been carried out within the framework of Hungarian-Italian Intergovernmental R&D (TéT)

Cooperation Project I-28/98 between the *Dipartimento di Meccanica e Aeronautica* - University of Rome “La Sapienza” and the *Department of Fluid Mechanics* - Technical University of Budapest. The author acknowledges MURST for the support under contract 447/1997. The author wishes also to acknowledge the hungarian colleagues, Prof. F. Bencze and Dr. J. Vad, for providing the data and for the helpful discussion.

References

Basson A., Kunz R. F. and Lakshminarayana B. (1993), "Grid generation for three-dimensional turbomachinery geometries including tip clearance", *J. Propulsion and Power*, 59:66.

Basson A. and Lakshminarayana B. (1995), "Numerical simulation of tip clearance effects in turbomachinery", *J. Turbomachinery*, 348:359.

Borello D., Corsini A., and Rispoli F. (1997a) "Prediction of Francis turbine runner performance using a 3-D finite element technique with unassembled stiffness matrix treatment", *2nd European Conf. on Turbomachinery*, Antwerp, 389:397.

Borello D., Corsini A., Rispoli F. (1997b), "A 3D stabilized finite element technique with compact stiffness matrix treatment. Application to internal flows", *ASME Paper FEDSM97-3491*.

Brooks A.N. and Hughes T.J.R. (1982), "Streamline Upwind/Petrov-Galerkin formulations for convection dominated flows with particular emphasis on the incompressible Navier-Stokes equations", *Comp. Meth. Appl. Mech. Eng.*, 199:259.

Corsini A. (1996), "Three dimensional analysis of turbulent flow behaviour inside a Francis turbine runner. Performance prediction using unassembled stiffness matrix finite element tecnique" (in Italian), *Ph. D. Thesis*, Università di Roma "La Sapienza".

Corsini A., Rispoli F., Vad J. and Bencze F. (1999) "Concerted experimental and numerical studies on axial flow fan rotor aerodynamics", *3rd European Conf. on Turbomachinery*, London, 519:531.

Craft T.J., Launder B.E., Suga K. (1993), "Extending the applicability of eddy viscosity models through the use of deformation invariants and non-linear elements", *5th IAHR – Refined Flow Modelling and Turbulence Measurements*, Paris, 125:132.

Dawes W. N. (1987), "A numerical analysis of the three-dimensional viscous flow in a transonic compressor rotor and comparison with the experiment", *J. of Turbomachinery*, 83:90.

Goyal R.K. and Dawes W.N. (1993), "A comparison of themeasured and predicted flow field in a modern by-pass configuration", *J. of Turbomachinery*, 273:282.

Hah C. (1984), "A Navier-Stokes analysis of three-dimensional turbulent flows inside turbine blade rows at design and off-design conditions", *J. of Engineering for Gas Turbines and Power*, 421:429.

Hansbo P., Johson C. (1995), "Streamline diffusion finite element methods for fluid flow", *VKI LS 1995-02*.

Hunter I.H. and Cumpsty N. A. (1982), "Casing wall boundary layer development through an isolated compressor rotor", *J. of Engineering for Gas Turbines and Power*, 805:818.

Inoue M. and Kuroumaru M. (1984), "Three-dimensional structure and decay of vortices behind an axial flow rotating blade row", *J. of Engineering for Gas Turbines and Power*, 561:569.

Inoue M. and Kuroumaru (1989), "Structure of tip clearance flow in an isolated axial compressor rotor", *J. of Turbomachinery*, 250:256.

Inoue M., Kuroumaru M., Iwamoto T. and Ando Y. (1991), "Detection of a rotating stall precursor in isolated axial flow compressor rotors", *J. of Turbomachinery*, 281:289.

Lakshminarayana B., Davino R. and Pouagare M. (1982), "Three-dimensional flow field in the tip region of a compressor rotor passage - part II: turbulence properties," *J. of Eng. For Power*, 772:781.

Launder B.E. (1995), "Advanced turbulence models for industrial applications", *Turbulence and Transition Modelling – ERCOFTAC/IUTAM*, 193:231.

Moyle I. N. (1989), "Influence of the radial component of the total pressure gradient on tip clearance secondary flow in axial compressors", *ASME Paper 89-GT-19*.

Rispoli F. and Siciliani F. (1994), "Una metodologia agli elementi finiti per il calcolo di flussi secondari incompressibili in condotti di turbomacchine" (in Italian), *49° Congresso Nazionale ATI*, Perugia, 1795:1807.

Saad Y. And Schultz M.H. (1986), "GMRES: a generalized minimal residual algorithm for solving nonsymmetric linear system", *SIAM J. of Stat. Comput*, 856:869.

Shakib F., Hughes T.J.R., Johan Z., 1989, “A multi element group preconditioned GMRES algorithm for nonsymmetric systems arising in finite element analysis”, *Comp. Meth. Appl. Mech. Eng.*, 415:456.

Speziale G.C., Younis B.A., Rubinstein R. and Zhou Y. (1998) "On consistency conditions for rotating turbulent flows", *Physics of Fluids*, 2108:2110.

Storer J.A. and Cumpsty N.A. (1991), "Tip leakage flow in axial compressors", *J. of Turbomachinery*, 252:259.

Tezduyar T.E. (1992) "Stabilized finite element formulations for incompressible flow computations", *Advances in Applied Mechanics*, Academic Press Inc..

Vad J. and Bencze F. (1996) "Secondary Flow in Axial Flow Fans of Non-Free Vortex Operation", *8th Int. Symp. Appl. of Laser Tech. Fluid Mech*, Lisbon, V.1.

Vad J. (1997) "Investigation on the flow field downstream of axial flow fans using Laser Doppler Anemometry" (in Hungarian), *Ph.D. Thesis*, Technical University of Budapest - Hungary.

Vad J. and Bencze F. (1998a), "Three-Dimensional Flow in Axial Flow Fans of Non-Free Vortex Design", *Int. J. of Heat and Fluid Flow*, 601:607.

Vad J. and Bencze F. (1998b), "Laser Doppler Anemometer Measurements Upstream and Downstream of an Axial Flow Rotor Cascade of Adjustable Stagger", *9th Int. Conf. on Flow Measurement (FLOMEKO)*, Lund, Sweden, 579:584.

Vad J. (1999), Private communication.

Notations

Latin letters

b	prescribed Neumann boundary conditions
C_p	static pressure coefficient
c_{e1}, c_{e2}	turbulent dissipation rate production constants
D	computational domain
d	prescribed Dirichelet boundary conditions
e_{ijm}	permutation tensor
$\boldsymbol{F}$	global force vector
f	residual forces vector
H	shape factor
h_{tip}	fraction of gap height from blade tip
K_B	blockage factor
k	turbulent kinetic energy
ℓ_{ch}	blade chord
n	normal vector components
P	production terms
p	pressure
r	radius
$R = r/r_c$	dimensionless radius
S_{ij}	strain tensor
U_c	reference velocity ($r_c \cdot$ w)
u	peripheral velocity
v	absolute velocity components
$\overline{w_i' w_j'}$	Reynolds stress tensor
w	relative velocity components

Greek letters

b_L	leakage flow angle
G	Prandtl turbulent numbers
g	blade stagger angle
d^+	dimensionless distance from wall
d	thickness of boundary layer at the edge
e	turbulent dissipation rate
z	auxiliary vector of the unknowns
J	vector of the unknowns
q	momentum thickness
l	angular position
m	dynamic viscosity
m_t	turbulent dynamic viscosity
n	kinematic viscosity
r	fluid density
s_j	diffusive flux vector
t_{ij}	stress tensor
j_a, j_r	local axial and radial flow coefficients
c	clearance
y	local ideal total head rise coefficient
W_{ij}	absolute vorticity tensor
w	rotor angular speed

Symbols

¶*D*	domain boundary
l.e.	leading edge
t.e.	trailing edge

Subscripts

c	casing end-wall
ch	chord
h	hub end-wall
i, j	Cartesian components
in	inertial forces
k	turbulent kinetic energy
L	leakage flow
m	momentum equation
r, p, a	radial, tangential, axial components
tip	blade tip
x, y, z	Cartesian components
a	index for degrees of freedom
e	turbulent dissipation rate
0	rotor inlet plane
1	free stream plane
3	rotor exit plane

Superscripts

0	total pressure
e	edge of the boundary layer
¯	averaged quantities
′	fluctuating quantities

Appendix

Design specifications of the investigated rotor (Vad and Bencze, (1996)) are summarized in Table A.1, together with the data describing the benchmark axial flow rotors (Inoue and Kuroumaru, (1984) and (1989)) and linear cascade (Storer and Cumpsty, (1991)).

	Inoue and Kuroumaru (1984)	*Inoue and Kuroumaru (1989)*	*Storer and Cumpsty (1991)*	*Vad and Bencze (1996)*
Vortex design	*free vortex*	*free vortex*		*non free vortex*
Hub-to-tip ratio	*0.6*	*0.6*	—	*0.676*
Span (mm)	*89.5*	*89.5*	*435*	*99.1*
Blade profile	*NACA 65*	*NACA 65*		*circular arc plate*
Blade thickness at the tip	$0.02\ \ell_{ch}$	$0.06\ \ell_{ch}$	$0.05\ \ell_{ch}$	$0.012\ \ell_{ch}$
Solidity at the tip	*0.5*	*1*	*1.7*	*1.047*
Chord lenght at the tip (mm)	*117.5*	*117.5*	*300*	*171*
Clearance	$0.006\ \ell_{ch}$	$0.017\ \ell_{ch}$	$0.02\ \ell_{ch}$	$0.018\ \ell_{ch}$
Tip stagger (deg)	*67*	*56.2*	*22.2*	*38.3*

Tab. A.1: design specifications of benchmark axial flow bladings